CHAPTER 6

Synthesis and photocatalytic applications of starch functionalized α-FeOOH/β-FeOOH /Cu_2O nanostructures

6.1 Introduction

Iron oxy-hydroxide nanostructures have unique chemical and physical properties with well-controlled shapes and sizes. Among the iron (III) oxy-hydroxide family, (n-type) goethite (α-FeOOH), (p-type) akaganéite (β-FeOOH), nanoparticles (NPs) are very stable and have been widely used as absorbents and catalysts in wastewater treatment. α-FeOOH and β-FeOOH have their bandgap in the visible range. The bandgap of α-FeOOH is ~ 2.2 – 2.9 eV and β-FeOOH is ~ 2.0 - 2.5 eV. Due to the relatively larger bandgap of α-FeOOH [He *et al.* (2002) and Wang *et al.* (2009)], β-FeOOH shows better visible light photocatalytic activity than the former [Xu *et al.* (2015)].

It is well established that composite heterostructures have better photocatalytic activity than corresponding pure phase materials. Thus, the visible-light photocatalytic activities of α-FeOOH and β-FeOOH have been further improved by surface modification and forming composites with other semiconductors [Liu *et al.* (2010), Shan *et al.* (2017), Wu *et al.* (2018) and Zhao *et al.* (2010)]. Nevertheless, there are only a few studies on α-FeOOH and β-FeOOH based heterojunction photocatalysts for the degradation of organic pollutants. For instance, Zhu *et al.* (2015) and Chowdhury *et al.* (2015) prepared β-FeOOH/TiO_2 heterostructure for different photocatalytic applications. After that, Fang *et al.* (2016) fabricated β-FeOOH coupled with single-walled carbon nanotubes to degrade methyl orange. Later, Chae *et al.* (2017) reported the Synthesis of β-FeOOH/Fe_3O_4 hybrid photocatalysts with high photocatalytic efficiency and good recyclability. Similarly, Malathi *et al.* (2017) prepared rod-on-flake α-FeOOH/BiOI heterojunction photocatalyst with enhanced photocatalytic efficiency and stability. Dong *et al.* (2018) and Zhao *et al.* (2020) demonstrated the Synthesis and photocatalytic application of α- FeOOH/g-C_3N_4 heterojunction. Similarly, Sun *et al.* (2018) reported rod-on-rod-like α-FeOOH/α-$AgVO_3$ heterostructures for degradation of organic pollutants

under visible light in an aqueous medium. More recently, He *et al.* (2020) and Wang *et al.* (2020) reported g-C_3N_4-Fe_3O_4/β-FeOOH heterostructures and β-FeOOH@g-C_3N_4 heterostructures. The prepared material was an efficient and stable photocatalyst for oxidizing organic contaminants.

In the previous chapter, the visible light catalytic activity of α-FeOOH/ β-FeOOH heterojunction has been demonstrated. The present chapter describes investigations on the visible light catalytic efficiency of α-FeOOH/ β-FeOOH/Cu_2O nanocomposites. The starting point is the starch functionalized α-FeOOH/ β-FeOOH nanocomposite prepared in Chapter 5. Since goethite is n-type and akaganéite is p-type; therefore, Cu_2O could be in contact with either of the two phases. The Fenton and visible light photo-Fenton activities of this unique p-n-p type β-FeOOH/α-FeOOH/Cu_2O nanocomposite were evaluated for the degradation of PNP and MO. A plausible mechanism for the improved photo-Fenton activity has been proposed.

6.2 Experimental Methods

6.2.1 Synthesis of starch functionalized α-FeOOH/ β-FeOOH (S2) nanocomposites

As discussed in section 5.2.1.

6.2.2 Synthesis of starch functionalized α-FeOOH/β-FeOOH/Cu_2O nanocomposites

Exactly 60 mg of the S2 nanopowder was redispersed in 60 mL water. An appropriate volume of 0.01 M aqueous solution of $CuNO_3$ (Merck) was then added to this suspension. In the next step, this suspension was agitated on a water bath shaker for 24 hours (until adsorption equilibrium). After 24 hours, the suspension was added in a drop-wise manner to 50 mL of 0.15 M NaOH with constant heating and stirring. The obtained reaction

mixture was heated at 60 °C with stirring for two more hours. This precipitate obtained (CSP) was washed several times with distilled water and dried at 50 °C in a hot air oven.

6.2.3 Photo-Fenton degradation of PNP over CSP

Precisely 50µL of the dispersed catalyst (1mg in 1mL distilled water) was added to 2 mL of PNP (0.2mL of 176µM diluted with 2 mL distilled water) solution at pH 3 in a standard quartz cuvette of 1cm path length. The pH of the PNP was maintained with the help of 0.1M HCl and 0.1 M NaOH. This suspension was kept for adsorption (for 60 minutes) until the achievement of equilibrium. Then, 30µL of 2M H_2O_2 (Merck) solution was added to this suspension. The cuvette was kept in a photocatalytic chamber under a cool white LED (approximately 1470 W/m^2) visible light source. The reaction was conducted both in the dark and under visible light. Hence, both Fenton and photo-Fenton activities of these nanocomposites were investigated.

6.2.4 Photo-Fenton degradation of MO over CSP

For catalytic degradation of MO over CSP, 50µL of the dispersed catalyst (1mg in 1mL distilled water) was added into 2mL of the 140µM solution of MO at pH 3. The suspension was allowed to stand until the achievement of adsorption (for 60 minutes) equilibrium. Next, 30µL of 2M H_2O_2 solution was added to the reaction mixture. The rest of the procedure was the same as that in the previous sub-section.

6.2.5 Characterization

Rigaku Miniflex 600 DTEXULTRA with Cu K_α radiation (λ=1.54 A°) was used for the powder XRD of the CSP sample. The scan rate was 10°/min in the range 10-90° of 2θ values. The data from the JCPDS powder diffraction files helped assign crystallographic planes to peaks in the XRD plots. FEI Technai-20 G^2 200 at the operating voltage of 200 kV was used for TEM and HR-TEM imaging. Solid-state UV-vis DRS

spectral measurements were recorded using the Shimadzu Pharmaspec UV-1700 model. Measurement of absorption spectrums (of PNP and MO under photo Fenton conditions) at regular intervals was done using Agilent Cary 60 UV-visible spectrophotometer.

6.3 Results and discussion

6.3.1 Characterization

Figure 6.1 compares the normalized powder X-ray diffraction patterns (XRD) of S2 and CSP nanocomposite. The XRD of CSP exhibited diffraction peaks due to goethite, akageneite, and cuprous oxide.

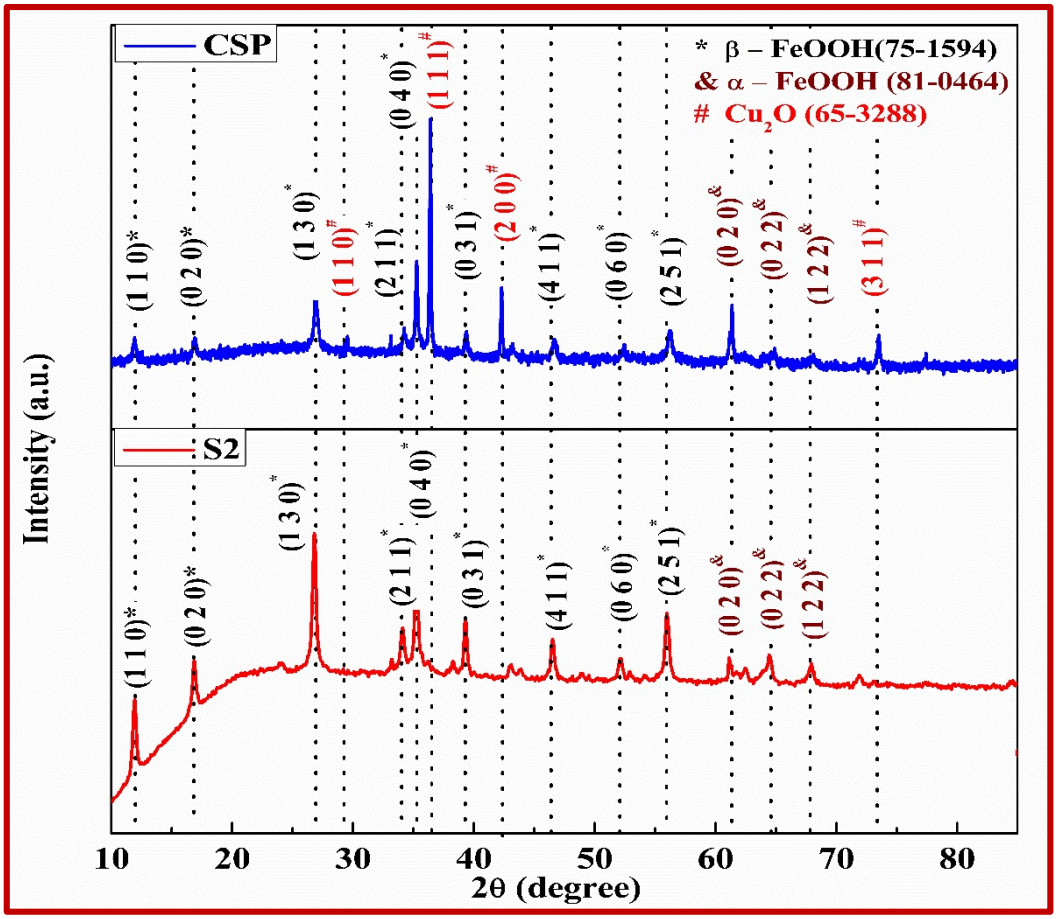

Figure 6.1 The X-ray powder diffraction pattern of S2 nanocomposite and CSP nanostructure powder samples.

TEM imaging revealed the morphological aspects of the prepared nanocomposite. The S2 nanocomposite has a rice-shaped nanostructure (Figure 5.3). After loading cuprous oxide, cubical nanostructures are formed over these rice-shaped nanoparticles(Figure 6.2a). The fringe spacing of HRTEM of CSP, 0.52 and 0.24 nm (Figure 6.2b) was indexed to the (0 2 0) and (1 1 1) lattice planes of akageneite (JCPDS: 75-1954) and cuprous oxide (JCPDS: 65-3288), respectively. Thus, the HRTEM analysis confirms the loading of cuprous oxide on the rice-shaped nanocomposites.

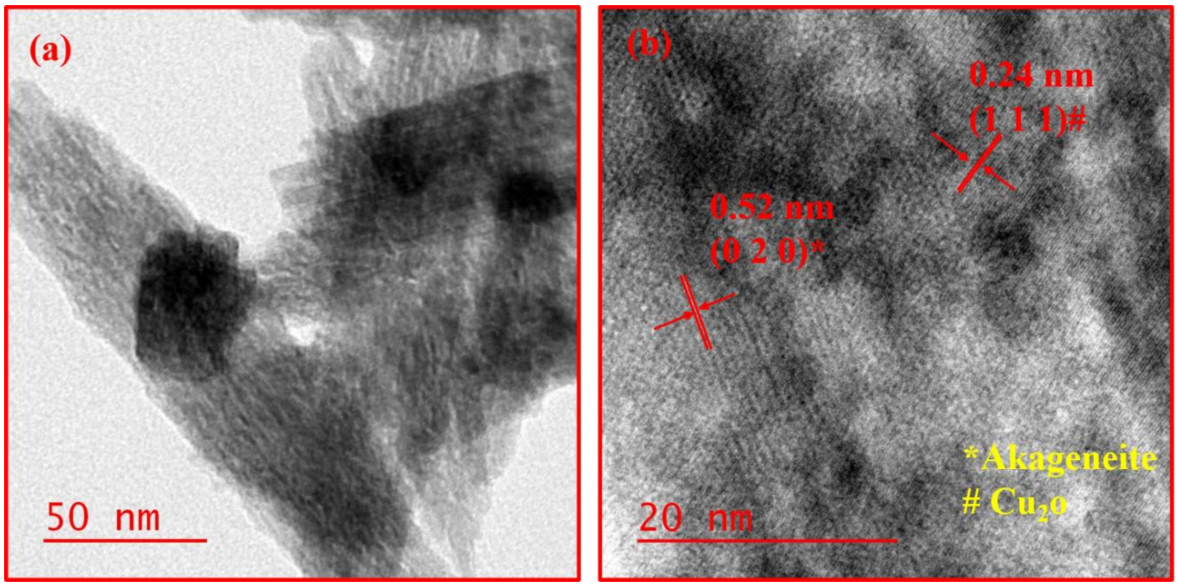

Figure 6.2 (a) Bright-field TEM image and **(b)** HR-TEM image of the CSP nanostructure.

XPS analysis of the CSP nanocomposite surface was also carried out (Figure 6.3). The Fe 2p peak showed the presence of Fe^{3+} following the fitting parameters for high-spin Fe^{3+} species by Biesinger and co-workers [Biesinger *et al.* (2011)]. Deconvoluted Fe 2p XPS spectra of CSP included four peaks centred at ~732.12, 723.3, 714.42, and 710.04 eV. These are attributed to Fe^{3+} in FeOOH, in agreement with the values reported earlier [Yang *et al.* (2017)]. The high-resolution XPS spectrum of Cu 2p exhibits peaks at 932.3

and 952.14 eV. These peaks, respectively, correspond to Cu 2p3/2 and 2p1/2 and confirm the presence of copper(I) oxide [Ghijsen *et al.* (1988)]. Deconvoluted O 1s XPS spectra revealed five peaks at ~528.3, 529.7, 531.4, 532.5, and 533.9 eV. The deconvoluted peak at 529.7 eV is due to the lattice oxide of cuprous oxide [Wang *et al.* (2018)]. Absorbed oxygen and lattice oxides in Fe–O–H, Fe–O–C, and C−O−C groups give rise to the rest of the peaks [Yang *et al.* (2017)].

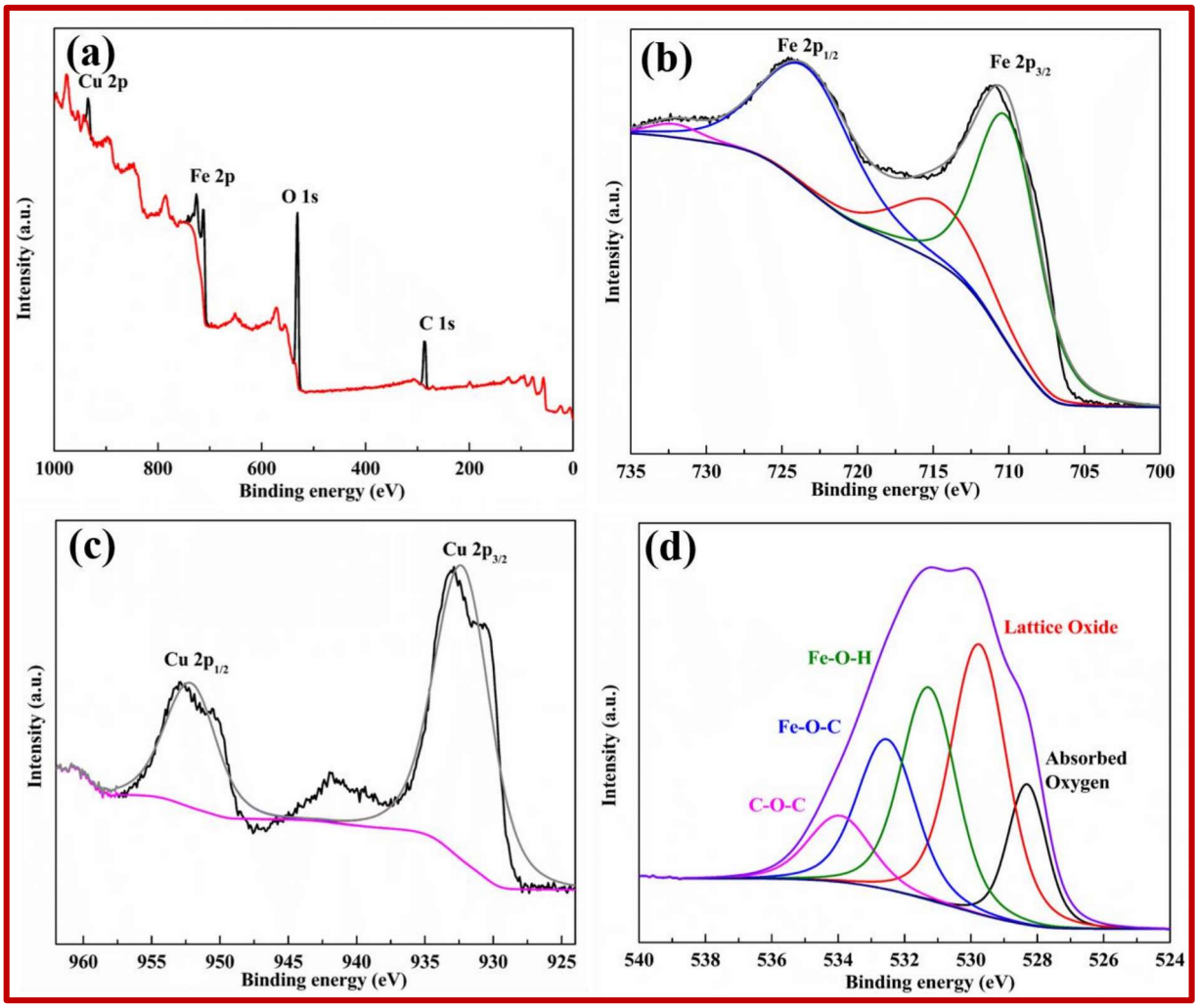

Figure 6.3 XPS analysis of CF (a) survey spectrum **(b)** Fe 2p, **(c)** Cu 3d, and **(d)** O 1s.

6.3.2 Optical band determination

It is necessary to evaluate the optical band gaps for understanding the photocatalytic mechanism. Tauc plot was derived from the normalized plot for solid UV-vis absorbance of CSP to investigate optical band gaps of CSP (Figure 6.4). The following equation gives the Tauc relation between the absorption coefficient alpha (α) and photonic energy (hυ):

$$\alpha = \frac{1}{h\upsilon}(h\upsilon - E_g)^n \text{ or } (\alpha h\upsilon)^{1/n} = h\upsilon - E_g \qquad (2.2)$$

In equation (2.2), α represents the molar absorption coefficient, n is the transition mode power factor, and E_g is the semiconductor's bandgap energy. The exponent n has a value of 0.5 for allowed direct transition and 2 for allowed indirect transition [Tumuluri *et al.* (2014)]. Figure 6.4a and 6.4b give the normalized solid UV-vis spectrum and their respective direct transition ($(\alpha h\upsilon)^2$ vs hυ) Tauc plots for CSP. The linear fit extrapolated to the (hυ) axis gave the value of optical bandgap energy. Three band gaps were clearly distinguished in the Tauc plot of sample CSP.

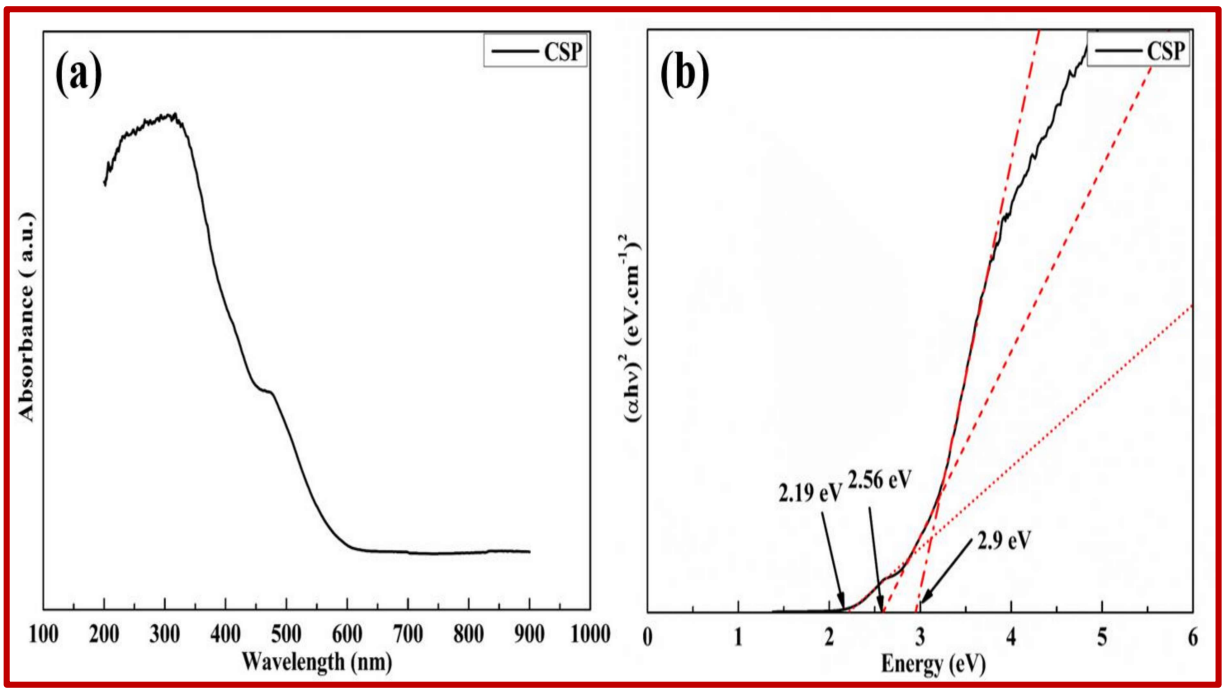

Figure 6.4 (a) solid state UV vis spectra of CSP nanostructure and **(b)** their respective Tauc plot.

To obtained the band edge positions of the components, the Mott–Schottky (MS) plots of CSP measured under dark condition (Figure 6.5). The MS plots of CSP exhibited one positive and two negative slope parts, confirming the formation of a p-n-p heterojunction. Flat band potential values obtained for CSP were +0.65 eV *vs.* NHE, +1.21 eV *vs.* NHE and +2.57 eV *vs.* NHE. The potential *vs.* Ag/AgCl reference electrode was converted to the potential *vs.* NHE by the relation $V(\text{NHE}) = V(\text{Ag/AgCl}) + 0.059\ \text{pH} + 0.197$ (here pH = 7).

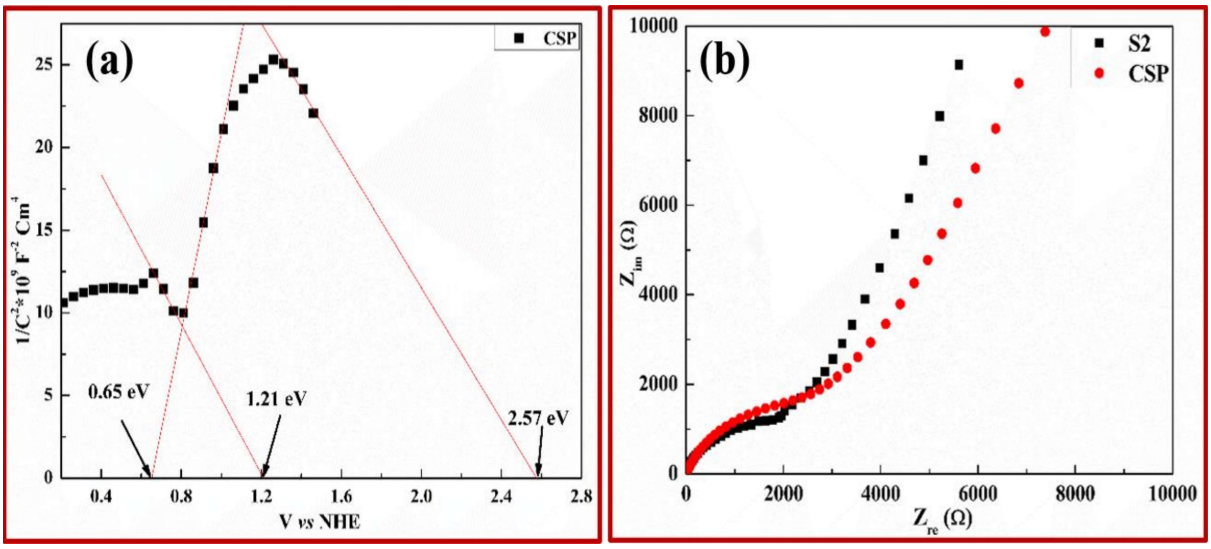

Figure 6.5 (a) The Mott Schottky plot of CSP measured under the dark condition in 0.5M Na_2SO_4 at 1 kHz and **(b)** the Nyquist plots of electrochemical impedance spectroscopy (EIS) for CSP and S2 for the investigation of the electron transfer kinetics of the catalysts.

Figure 6.6 represents the bandgap and band edge position of components constituting the CSP before and after the formation of p-n-p heterojunction. Part b of the same figure shows the change in the relative positions of these band edges of CSP, which is a composite of S2 nanocomposite and Cu_2O nanostructures. The formation of p-n-p junction shifts the positions of respective band edges. The Nyquist plots of electrochemical impedance spectroscopy (EIS) of S2 and CSP are given in Figure 6.5b. Both the samples show almost the same electron transfer kinetics.

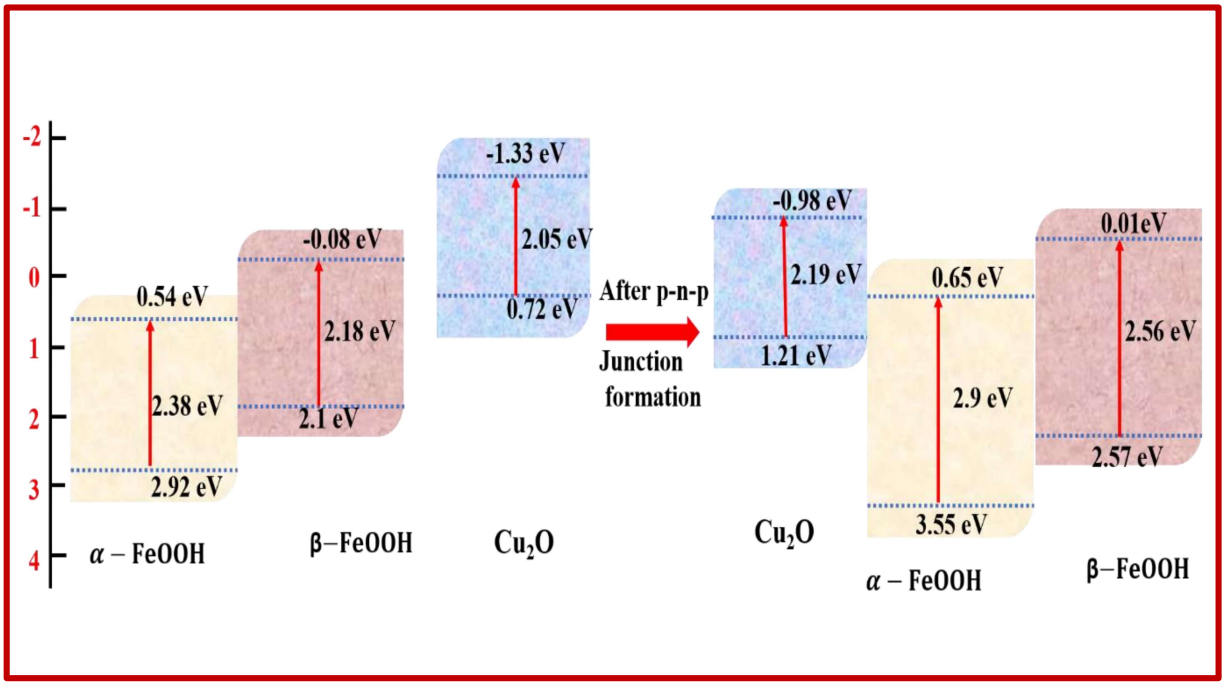

Figure 6.6 Band edges and band gap values of components of CSP before and after the formation of p-n-p heterojunction.

6.3.3 Photo-Fenton degradation of PNP and MO over CSP

Figure 6.7 and 6.8 shows the UV-vis spectrum of the Fenton and photo-Fenton degradation of PNP and MO over CSP catalyst. The rate of PNP and MO degradation over CSP under visible light was higher than that observed in the absence of light. The differential rate law equation was used to investigate the kinetics of PNP and MO degradation catalyzed by CSP as described in section 4.3.3.

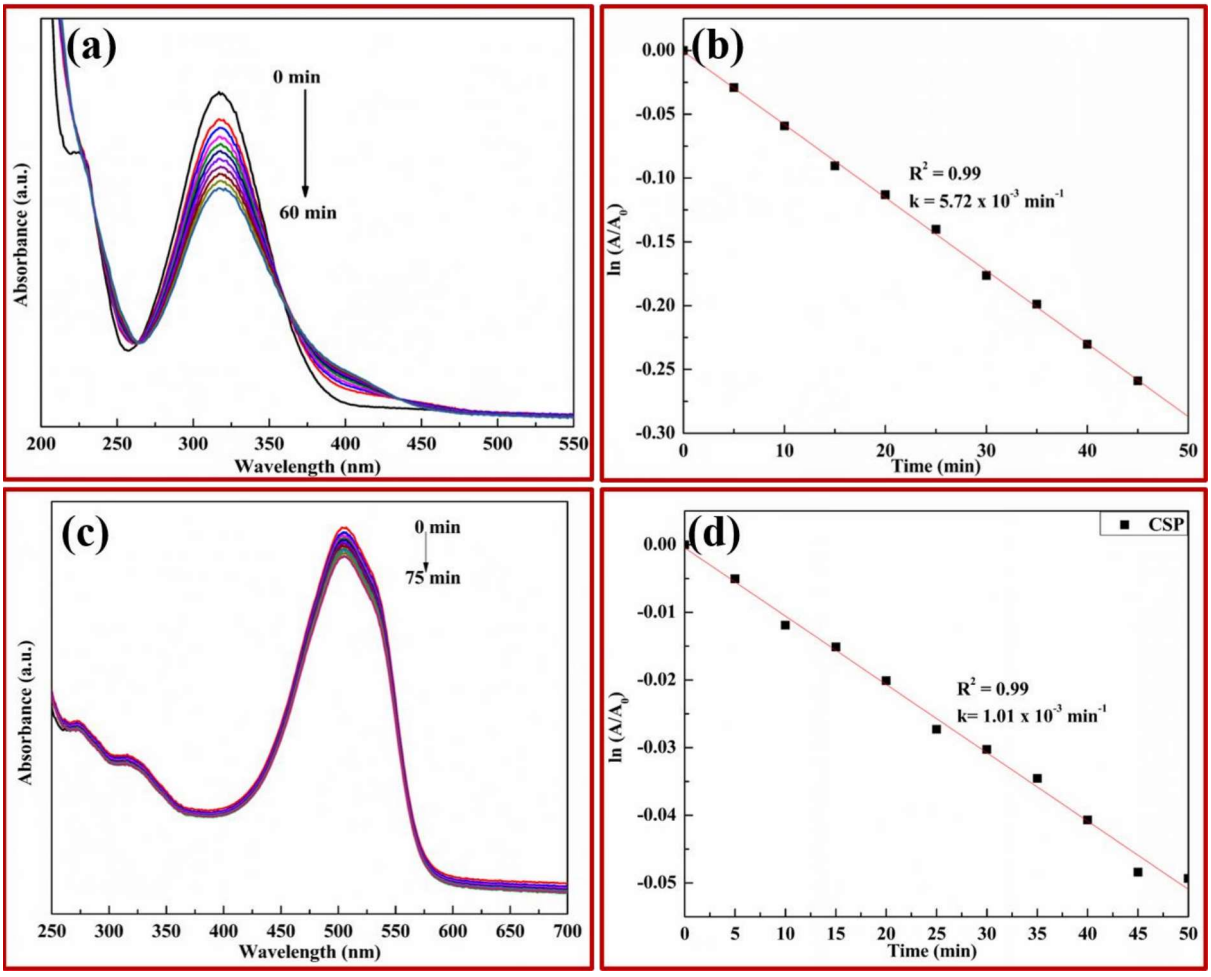

Figure 6.7 (a, c) UV-Visible plot for the Fenton degradation (dark condition) of PNP and MO as a function of reaction time under the optimum reaction conditions by CSP catalytic sample **(b, d)** rate kinetics plots of PNP and MO degradation using CSP catalyst.

The Fenton degradation of PNP and MO catalyzed by CSP follows first order rate kinetics. In contrast, the photodegradation of PNP and MO catalyzed by CSP follow pseudo-zero order rate kinetics. Figure 6.7b and 6.7d represents the $ln\left(\frac{A_t}{A_o}\right)$ versus t plots while figure 6.8b and 6.8d presents $\left(\frac{A_t}{A_o}\right)$ Versus t plots for Fenton and photo Fenton degradation of PNP and MO in the presence of CSP respectively. Here A_o and A_t are the initial and final concentrations of pollutant at time t = 0 and t respectively. Nearly perfect linear fits were obtained in both cases. The rate constant (k_{app}) was derived from the slope

of the linear fits to the respective plot. The rate of reaction was faster in the presence of light.

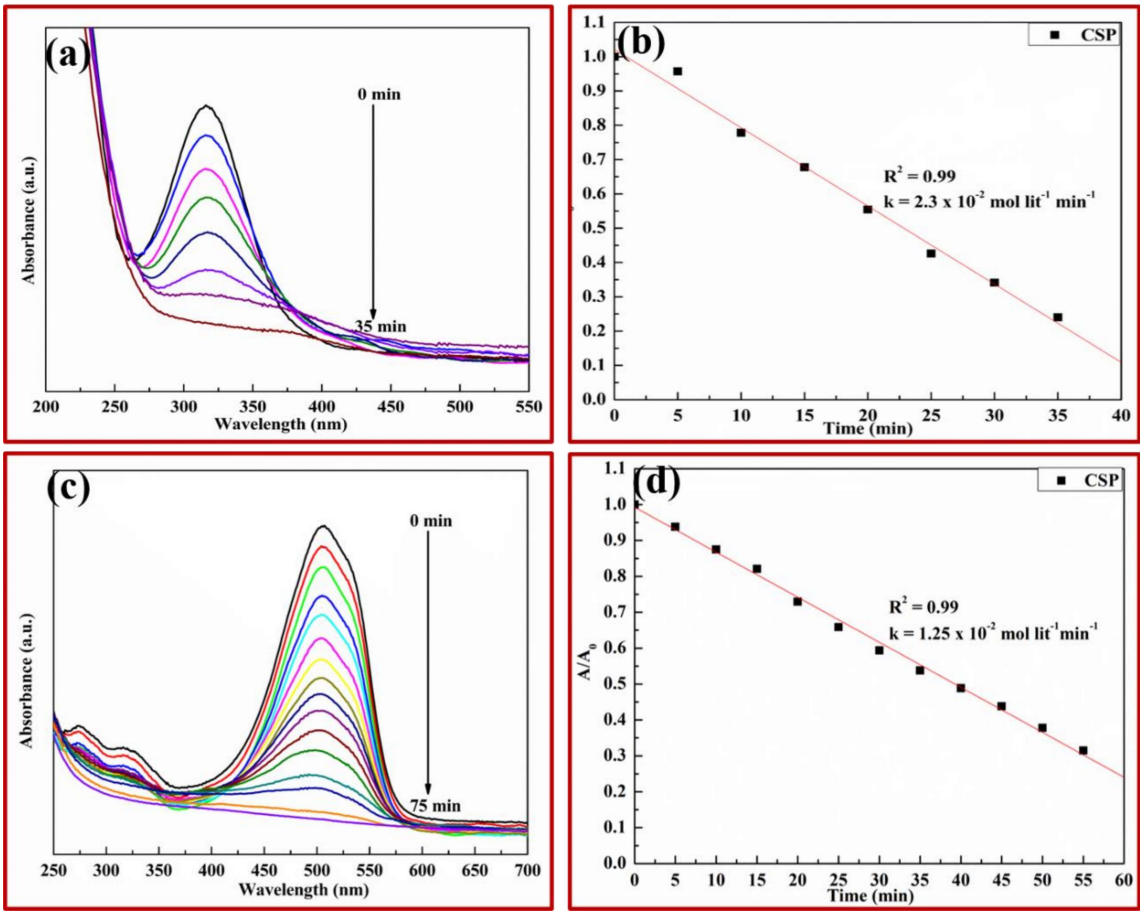

Figure 6.8 (a, c) UV-Visible plot for the photo-Fenton degradation of PNP and MO as function of reaction time under the optimum reaction conditions by CSP catalytic sample **(b, d)** rate kinetics plots of PNP and MO degradation using CSP catalyst.

The catalytic activity of CSP was determined by calculating the TOF using equation 4.4. Table 6.1 and 6.2 compares the TOF value for photo-Fenton degradation of PNP and MO in the presence of CSP with other photocatalysts reported in the literature. Most of the researcher reported the photocatalysts which are activated in the presence of UV light or higher intensity visible light sources. The TOF value obtained for Photo-Fenton degradation of PNP and MO using CSP catalyst was higher than the TOF values obtained for other catalysts.

Table 6.1 Comparison of TOF values for Photo-Fenton degradation of PNP in the presence of different catalysts studied earlier in literature with ones investigated in this work.

Catalyst	Light Source	TOF (moles $gram^{-1}$ min^{-1}	Reference
CSP	Cool white LED (0.1470 W/cm^2, visible range light source)	2.01×10^{-5}	This work
FeVO4@BiOCl	UV (shortwave, 254 nm, 8 W)	9×10^{-6}	Eshaq *et al.* (2020)
Cu/Fe-AO-PAN fiber	500 W Xenon lamp	2.03×10^{-7}	Wang *et al.* (2019)
CuO/Al_2O_3	Microwave irradiation of 100 W power	8.2×10^{-7}	Pan *et al.* (2015)
$GO\text{-}Fe_2O_3$	300W Dy Lamp (420nm visible light source)	2.5×10^{-6}	Guo *et al.* (2013)

Table 6.2 Comparison of TOF values for photodegradation of MO in the presence of different catalysts studied earlier in literature with ones investigated in this work.

Catalyst	Light Source	TOF (moles $gram^{-1}$ min^{-1})	References
CSP	Cool white LED (0.1470 W/cm^2, visible range light source)	7.5×10^{-5}	This work
$CuCr_2O4/CeO_2$	50 W cool white LED	1.99×10^{-7}	Ghorai *et al.* (2021)
α-FeOOH QDS/g-C_3N_4	500 W Xe lamp with UV cutoff filter (> 420 nm)	5.09×10^{-5}	Qian *et al.* (2018)
$\alpha\text{-}Fe_2O_3/Bi_2WO_6$	UV light (ca. 90 W/m^2)	2.03×10^{-6}	Jaramillo-Páez *et al.* (2017)
TiO_2/ β-FeOOH	Visible light(500 W xenon lamp and UV light (Hg Lamp)	8.76×10^{-6}(VL) 9.88×10^{-6} (UV)	Xu *et al.* (2013)

6.3.4 Recyclability test

The recyclability of CSP sample was also studied to check the stability of catalytic sample. No significant loss of activity was observed thus confirming that the CSP system was very stable during the degradation process, even after 5th cycle (Figure 6.9).

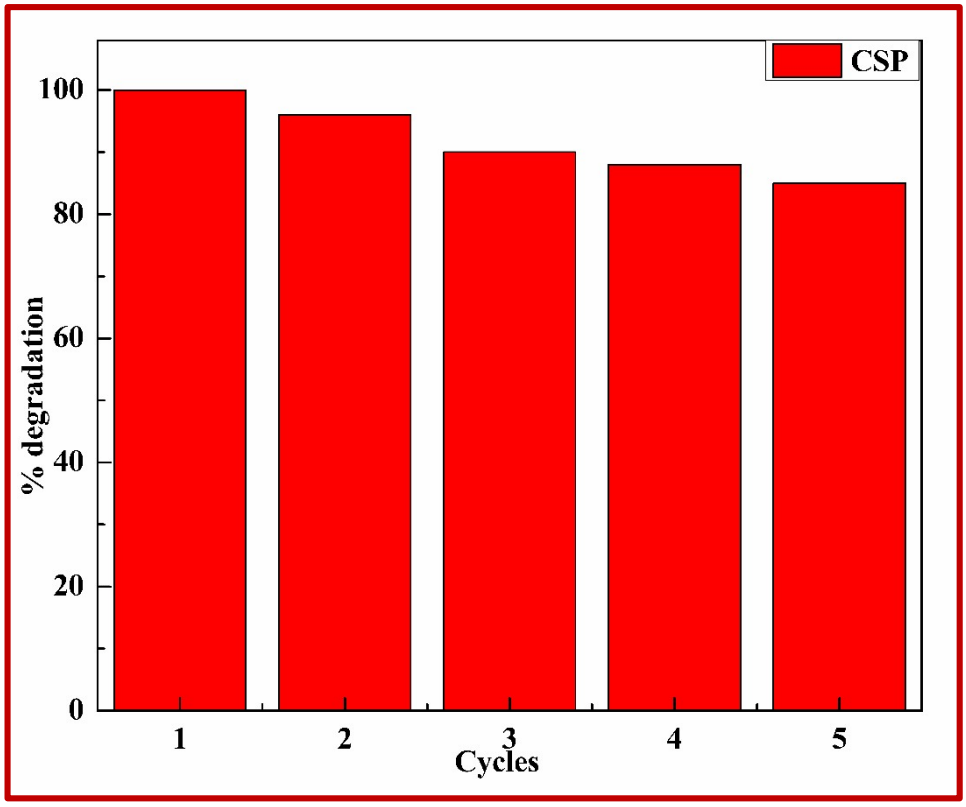

Figure 6.9 Five cycles of CSP reusability results in histogram format for PNP degradation for 1 hour.

6.3.5 Photocatalytic mechanism

Figure 6.10 shows the plausible mechanism for H_2O_2 degradation over CSP catalyst. The MS plot confirms the formation of p-n-p heterojunction. When CSP catalyst was irradiated with light the all the components get excited. Following the p-n-p mechanism, the electrons from CB of β-FeOOH and Cu_2O transferred into the CB of α-FeOOH and gets accumulated there. The holes from the VB of α-FeOOH migrated into the VB of β-FeOOH and Cu_2O. The oxidation of hydrogen peroxide to peroxyl radical

occurs on the VB of β-FeOOH. On the other hand, electrons excited to the CB of α-FeOOH are consumed by the reduction of hydrogen peroxide and consequent formation of hydroxyl radicals and hydroxide ion. The hydroxide ion further oxidized to hydroxyl radicals by holes excited to the Cu_2O. The hydroxyl radicals are potent oxidizing species which oxidizes the organic pollutant into carbon dioxide and water.

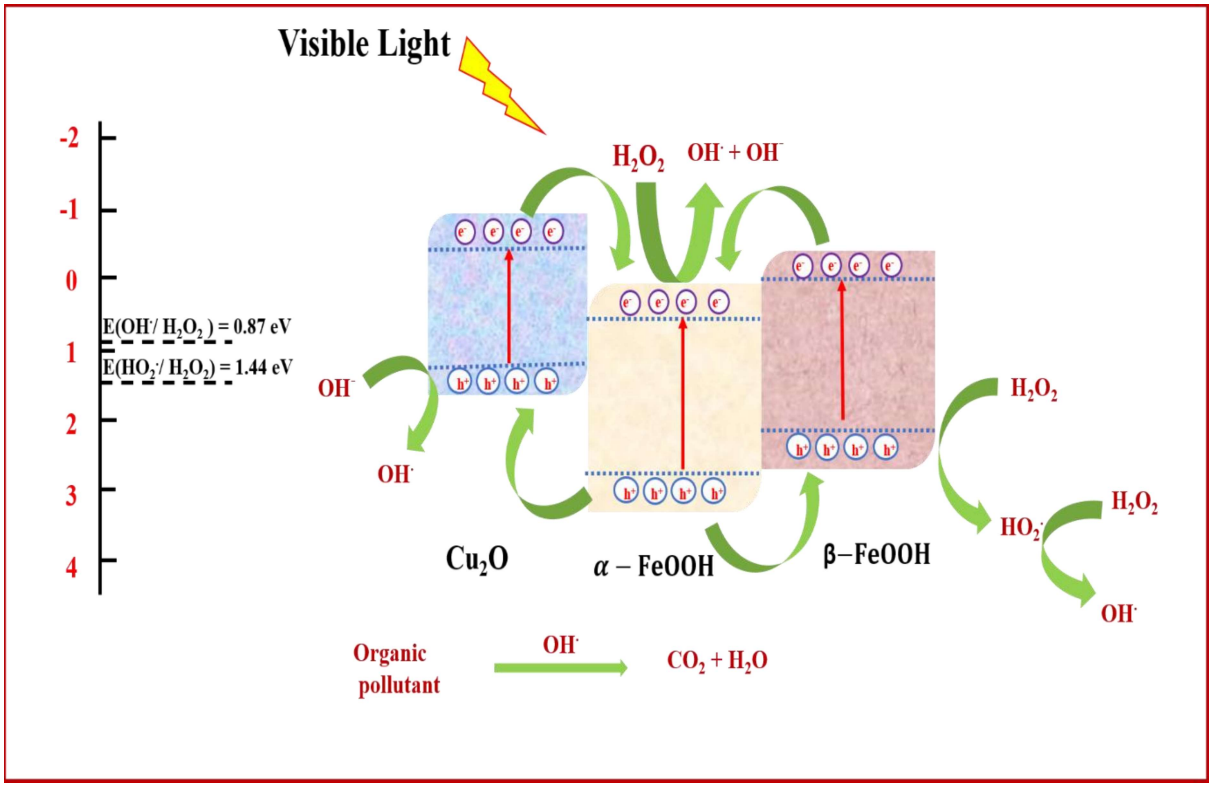

Figure 6.10 Schematic representation of the mechanism proposed for explaining the photo- Fenton degradation of organic pollutants.

6.4 Conclusions

The starch functionalized nanocomposites of goethite, akageneite and Cu_2O were prepared by green synthesis methodology. The nanocomposites were p-n-p heterojunction of goethite, akageneite and Cu_2O. The nanocomposite shows enhanced catalytic activity towards photo-Fenton degradation of PNP and MO. The p-n-p charge

separation mechanism led to the accumulation of electrons on the CB of goethite, while the holes got migrated on the VB of akageneite and Cu_2O part of these nanocomposites. The formation of p-n-p heterojunction enhances the charge separation in CSP, thus results in the increased photocatalytic activity.